Check for updates

Angewandte Chemie

Angewandte Chemie GDCh German Chemical Society

Zitierweise: *Angew. Chem. Int. Ed.* **2026**, e9899225
doi.org/10.1002/anie.9899225

FORSCHUNGSARTIKEL

Two-Dimensional Mesoporous Tungsten Oxynitride/Carbon Nanosheets: Enabling High-Performance Lithium-Sulfur Batteries

Zhenwen Li[1] | Ruiming Liu[1] | Qun Chen[1] | Mingjian Wen[1] | Xiaodan Huang[2] | Qin Yue[1]

[1]Institute of Fundamental and Frontier Sciences, University of Electronic Science and Technology of China, Chengdu, P. R. China | [2]Australian Institute for Bioengineering and Nanotechnology, The University of Queensland, Brisbane, Australia

Correspondence: Mingjian Wen (mjwen@uestc.edu.cn) | Qin Yue (qinyue@uestc.edu.cn)

Received: 4 December 2025 | **Revised:** 19 March 2026 | **Accepted:** 11 April 2026

Keywords: electrocatalyst | lithium-sulfur battery | polysulfide conversion | tungsten oxynitride

ABSTRACT

Lithium-sulfur batteries (LSBs) hold great promise as next-generation energy storage devices, owing to their ultrahigh theoretical energy density (2600 Wh kg^{-1}). However, their real-world implementation is limited by the polysulfide shuttle effect and the poor electrical conductivity of sulfur species. To address these problems and achieve high-performance LSBs, it is crucial to develop multifunctional catalysts featuring abundant active sites, short and accessible ion transport channels, and lightweight architectures. Herein, a novel two-dimensional mesoporous tungsten oxynitride/carbon nanosheet (WNO-MCS) material is successfully fabricated via a self-template-guided interfacial assembly strategy. The resulting WNO-MCS exhibits a uniform two-dimensional nanosheet morphology, featuring vertically aligned mesoporous channels across the sheets with a pore size of 3.9 nm, a high surface area of 588.7 m^2 g^{-1}, and well-confined WNO nanoclusters (~2.9 nm) embedded in the mesopores. This unique 2D mesoporous structure provides short, open pathways for ion transport and highly exposed active sites; thus, LSBs with a WNO-MCS-modified separator deliver a remarkable areal capacity of 7.7 mAh cm^{-2} under a high sulfur loading of 8.0 mg cm^{-2}. Moreover, the pouch cell achieves an initial discharge capacity of 0.62 Ah with a high energy density of 360 Wh kg^{-1}.

1 | Introduction

Lithium-sulfur batteries (LSBs) are recognized as promising candidates for next-generation energy storage due to their high theoretical energy density of 2600 Wh kg^{-1}, cost-effectiveness, and environmental sustainability [1–3]. Despite their potential, the commercialization of LSBs is impeded by several key issues, including the shuttle behavior of lithium polysulfides (LiPSs), the poor conductivity of sulfur and its discharge products (e.g., S: ~5×10^{-30} S cm^{-1}; Li_2S: ~1×10^{-9} S cm^{-1}), and sluggish conversion kinetics between sulfur, LiPSs, and Li_2S [4–6]. To overcome these limitations and improve the energy density, cycling stability, and rate capability, the introduction of functional metallic catalysts into host materials or separator modifications has been widely investigated [7–9]. These catalysts enhance the conversion kinetics of LiPSs through strong chemical interactions, offering a viable route toward high-performance LSBs [10–13].

Tungsten-based materials, with their tunable electronic structures and multiple accessible oxidation states (0–6), exhibit excellent electrocatalytic properties and chemical versatility, making them attractive for LiPSs regulation [14–17]. For instance, tungsten oxides such as WO_3 possess Lewis acid sites that strongly adsorb LiPSs via electron transfer between W/O centers and S^{2-}/Li^+ species [18–20]. To address the intrinsic low conductivity and sluggish redox kinetics of WO_3, hybrid structures like

© 2026 Wiley-VCH GmbH

WC-WO_3/C and WS_2-WO_3 have been developed, which demonstrate improved catalytic activity toward LiPSs conversion [21, 22]. However, conventional synthesis often involves high-temperature treatments that lead to particle aggregation and phase separation due to Ostwald ripening. This results in oversized inactive particles that increase the electrode weight without contributing to the capacity, thereby reducing the overall energy density and limiting synergistic catalytic effects. Face-centered cubic tungsten oxynitride (WNO), a nitrogen-substituted derivative of WO_3, exhibits enhanced electrical conductivity and stronger adsorption toward LiPSs while maintaining rich active sites, representing a promising catalytic material for LSBs [23, 24]. However, its synthesis typically requires hazardous ammonia nitridation steps, and few reports exist on rationally designed WNO-based architectures that simultaneously maximize catalytic activity, facilitate ion transport, and minimize weight—all critical for practical high-energy density LSBs.

Herein, we present a straightforward self-templating method for the in situ fabrication of ultrafine WNO nanoclusters confined within two-dimensional mesoporous carbon nanosheets (denoted as WNO-MCS). In this approach, two-dimensional WO_3 nanosheets serve simultaneously as a structural template and a tungsten source. Through interfacial polymerization of dopamine and co-assembly with surfactant micelles in an alkaline ammonia solution, WO_3 is gradually etched, allowing tungsten species to coordinate with amino groups and incorporate into a polymer-micelle mesostructure. After carbonization, ultrafine WNO nanoclusters (~2.9 nm) are homogeneously embedded within vertically aligned mesoporous carbon nanosheets with a pore size of ~3.9 nm. The resulting hierarchical architecture offers short, open ion diffusion pathways, fully exposed active sites with specific surface area of 588.7 m^2 g^{-1}, and effective nanoconfinement that stabilizes the WNO clusters. When applied as a separator modifier in LSBs, WNO-MCS enables an original discharge capacity of 1424.6 mAh g^{-1} at 0.2 C, permanent performance over 500 cycles at 1 C, and exceptional rate capability (798.4 mAh g^{-1} at 5 C). Notably, pouch cells fabricated with this modifier deliver an Ah-level capacity and a favorable energy density of 360 Wh kg^{-1}, highlighting their potential as a competitive alternative to conventional lithium-ion batteries.

2 | Results and Discussion

Scheme 1 illustrates the synthesis of two-dimensional WNO-MCS and its application as a functional modifier on LSBs separators. Uniform WO_3 nanosheets with a thickness of 9.6 nm are prepared through the hydrothermal method (Figure S1), which are used as both self-sacrificial templates and tungsten sources. In an alkaline ammonia environment, dopamine undergoes polymerization, and the resulting polydopamine oligomers co-assemble with TMB-swollen spherical F127 micelles via hydrogen bonding. The assembly deposits uniformly on the WO_3 nanosheets. Concurrently, WO_3 is gradually etched by ammonia, releasing W species that coordinate with the amino groups of polydopamine and incorporate into the growing mesostructure. After annealing, ultrafine WNO nanoclusters are successfully confined within the obtained two-dimensional mesoporous carbon nanosheets.

To elucidate the formation mechanism, we examined reaction intermediates collected at different time intervals by transmission electron microscopy (TEM). As illustrated in Figure S2a,b, within the first half-hour, polydopamine (PDA) adheres to the WO_3 nanosheet surfaces via dipole-dipole interactions and undergoes interfacial epitaxial growth. When the reaction proceeds beyond 1 h (Figure S2c,d), the WO_3 templates gradually etch and reduce in size due to their reaction with NH_4OH, forming water-soluble ammonium tungstate which serves as the tungsten source. After 2 h, the WO_3 templates were fully dissolved, and the cross-linked W/PDA/F127 mesostructure was fixed (Figure S2e,f). Following freeze-drying, the resulting W/PDA/F127 exhibits ultrathin two-dimensional nanosheets with well-defined mesopores (Figures 1a-i and S3). Subsequent annealing in an Ar atmosphere decomposes the F127 and carbonizes the PDA, leading to the formation of mesoporous carbon nanosheets. Concurrently, the confined tungsten species were nitrided by nitrogen-containing functional groups from dopamine, yielding uniformly dispersed WNO nanoclusters embedded within the mesoporous channels, denoted as WNO-MCS.

Scanning electron microscopy (SEM) images of WNO-MCS (Figures 1a-ii and S4) show a well-preserved two-dimensional nanosheet morphology with clearly visible, vertically aligned mesoporous channels approximately 4.0 nm in diameter. These uniform, open mesopores provide ample space for LiPSs immobilization and significantly enhance ionic diffusion kinetics, thereby facilitating Li^+ transport. Furthermore, high-resolution transmission electron microscopy (HRTEM) images (Figure 1a-iii) reveal numerous ultrafine nanoclusters (~2.9 nm in diameter) uniformly dispersed within the mesopores of WNO-MCS. The clearly resolved lattice spacing of 0.24 nm corresponds to the (111) plane of $W_{0.62}$[N,O] (Figure 1a-iv). Figure 1a-v displays polycrystalline diffraction rings observed in selected area electron diffraction (SAED), which are indexed to the (111), (200), (220), and (311) planes of $W_{0.62}$[N,O]. The elemental mapping of energy-dispersive x-ray spectroscopy (EDS, Figure 1b) further proves the uniform distribution of $W_{0.62}$[N,O] within the pore structure of MCS. To clarify the structure-directing role of WO_3 templates, mesoporous polydopamine (mPDA) was synthesized and subsequently carbonized into mesoporous carbon (MC) in the absence of WO_3 templates. SEM and TEM images (Figure S5) reveal that without WO_3, the resulting structure exhibits typical spherical mesoporous morphology, underscoring the essential templating effect of WO_3 nanosheets in forming the two-dimensional architecture.

The x-ray diffraction (XRD) pattern of MC (Figure 1c) displays broad peaks at 24.0° and 43.7°, attributed to the (002) and (101) planes of graphite [25]. In contrast, the XRD pattern of WNO-MCS shows distinct and sharp diffraction peaks that align well with the standard $W_{0.62}$[N,O] phase (JCPDF No. 25–1254), confirming the successful incorporation of pure-phase $W_{0.62}$[N,O] into the carbon framework. N_2 adsorption-desorption isotherms (Figure 1d) are consistent with the standard type-IV curve and present the H3 hysteresis loop, which is characteristic of mesoporous materials. Pore size distributions (Figures 1d and S6) indicate a uniform pore diameter centered at 3.9 nm for both WNO-MCS and MC microspheres. Notably, WNO-MCS possesses a higher specific surface area (588.7 m^2 g^{-1}) than MC (560.6 m^2 g^{-1}), which is attributed to its two-dimensional nanosheet architecture that

15213757, 0, Downloaded from https://onlinelibrary.wiley.com/doi/10.1002/ange.9899225 by University Of Electronic Science And Technology Of China, Wiley Online Library on [24/04/2026]. See the Terms and Conditions (https://onlinelibrary.wiley.com/terms-and-conditions) on Wiley Online Library for rules of use; OA articles are governed by the applicable Creative Commons License

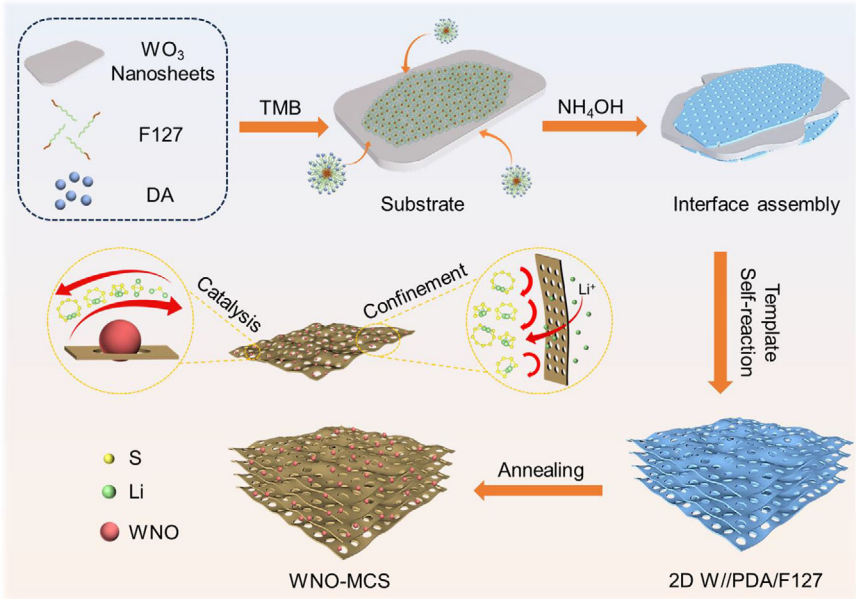

SCHEME 1 | Schematic illustration of the synthesis process of WNO-MCS.

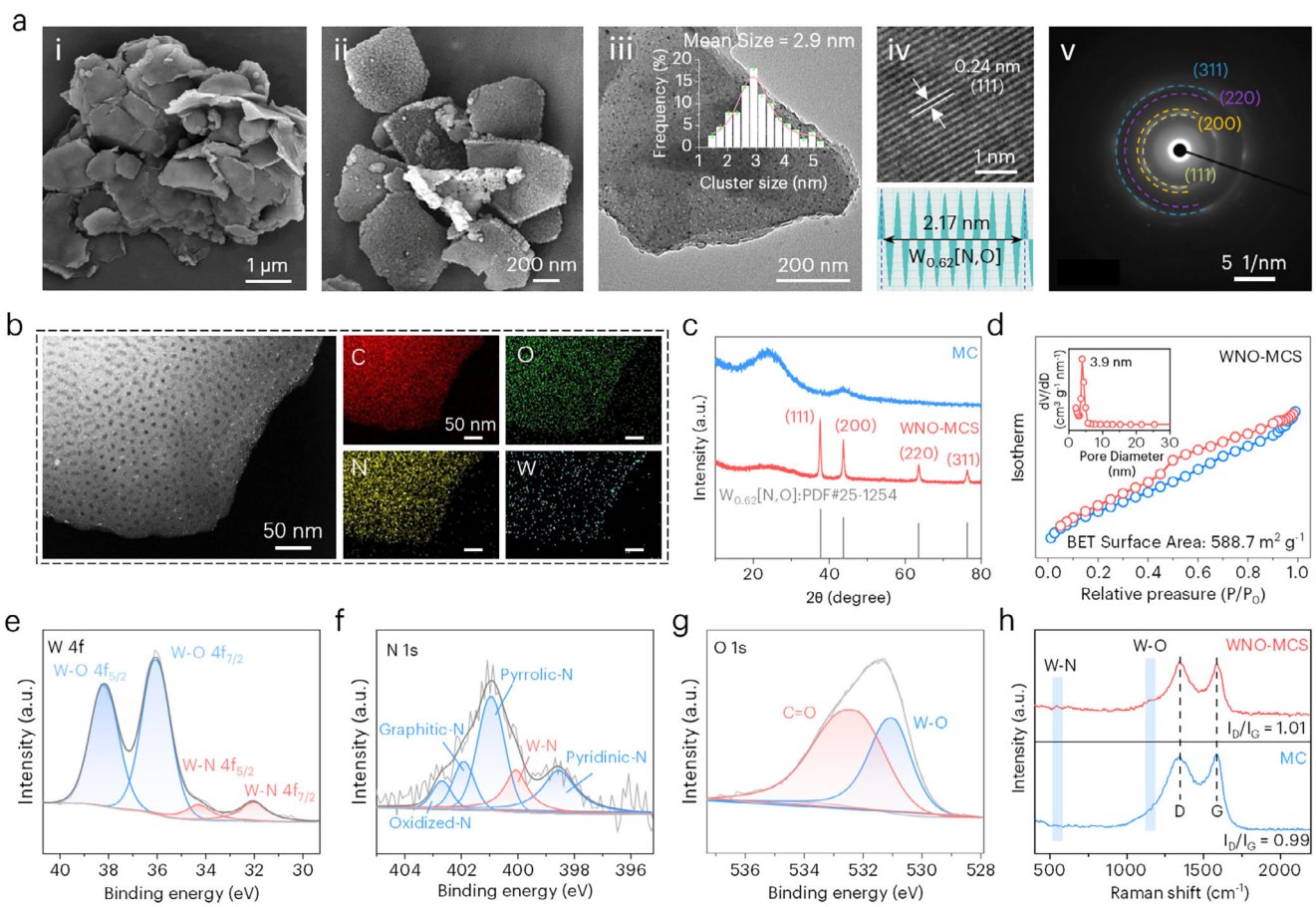

FIGURE 1 | Material characterization of WNO-MCS. (a) Morphological characterization. (i) SEM image of the W/PDA/F127 precursor. (ii) SEM, (iii) HRTEM images (inset: WNO nanocluster size distribution), (iv) lattice fringes, and (v) SAED image of WNO-MCS. (b) HAADF-STEM images and corresponding EDS element maps of WNO-MCS. (c) XRD patterns of MC and WNO-MCS. (d) N_2 adsorption-desorption isotherms of WNO-MCS (inset: pore size distributions). XPS spectra of (e) W 4f, (f) N 1s, and (g) O 1s of WNO-MCS. (h) Raman spectra of MC and WNO-MCS.

15213757, 0, Downloaded from https://onlinelibrary.wiley.com/doi/10.1002/ange.9899225 by University Of Electronic Science And Technology Of China, Wiley Online Library on [24/04/2026]. See the Terms and Conditions (https://onlinelibrary.wiley.com/terms-and-conditions) on Wiley Online Library for rules of use; OA articles are governed by the applicable Creative Commons License

provides more accessible mesopores and shortened diffusion pathways. The chemical state of WNO-MCS was explored by x-ray photoelectron spectroscopy (XPS). Figure 1e illustrates four peaks at 32.1, 34.3, 36.0, and 38.2 eV in the high-resolution W 4f spectrum. The first two peaks are attributed to the W-N bond, while the latter two are linked to the W-O bond [26, 27]. The N 1s spectrum (Figure 1f) can be deconvoluted into five components: pyridinic N (398.6 eV), W-N (400.1 eV), pyrrolic N (400.9 eV), graphitic N (401.9 eV), and oxidized N (402.7 eV) [28]. Similarly, the O 1s spectrum (Figure 1g) displays peaks at 531.0 eV (lattice O^{2-} in W-O) and 532.3 eV (C = O) [29]. Furthermore, the C 1s spectrum (Figure S7) shows contributions from sp^2 C (284.8 eV), sp^3 C (285.9 eV), C = O/C-N (287.2 eV), and π-π* satellites (289.2 eV) [30].

Raman spectroscopy was utilized to assess the structural disorder and crystallinity of the mesoporous carbon samples (Figure 1h). The Raman spectrum of WNO-MCS, in contrast to that of MC, exhibits distinct peaks at 1172.6 and 545.2 cm^{-1}, characteristic of W-O and W-N vibrations, respectively. This confirms the presence of tungsten nitride/oxide phases [31]. Both samples show distinct G and D bands at 1587.3 and 1344.1 cm^{-1}, matching the in-plane vibration of sp^2-bonded carbon and the disordered sp^3-hybridized carbon, respectively [32]. Notably, the calculated ID/IG ratio for WNO-MCS (1.01) is larger than that for MC (0.99), suggesting that the incorporation of WNO can induce the carbon matrix to shift toward a defect-rich structure, thereby generating extra accessible active centers.

The adsorption capability of WNO-MCS and MC toward Li_2S_6 was evaluated using ultraviolet-visible (UV-vis) spectroscopy. After immersing the samples in a 5 mM Li_2S_6 solution for 0.5 h (Figure 2a), the solution with WNO-MCS shows nearly complete decolorization, indicating strong adsorption, whereas the solution with MC remains light yellow, suggesting weaker adsorption. UV-vis spectra further confirm the superior Li_2S_6 uptake by WNO-MCS. To elucidate the chemical mechanism underlying the adsorption of Li_2S_6 by the adsorbent, XPS measurements were conducted on WNO-MCS before and after Li_2S_6 adsorption. The S 2p spectrum of pristine Li_2S_6 (Figure 2b) displays four fitted peaks at 162.3, 164.9, 168.2, and 170.0 eV, assigned to terminal sulfur (S_T^{-1}), bridging sulfur (S_B^0), sulfite, and sulfate, in that order [33, 34]. Upon adsorption, all S 2p peaks shift to higher binding energies in WNO-MCS@Li_2S_6, while the W 4f peaks shift to lower energies (Figure 2c), indicating electron transfer from Li_2S_6 to the WNO sites. Furthermore, a new Li-N peak (56.2 eV) can be observed on the Li 1s spectrum of WNO-MCS@Li_2S_6 (Figure S8a), and the characteristic pyridinic-N and W-N peaks in the N 1s spectrum (Figure S8b) shift downward by approximately 0.3 and 0.4 eV, respectively [35]. These results demonstrate that, in addition to the WNO active centers, the polar nitrogen dopants in the carbon matrix also participate in chemical interactions with Li_2S_6, collectively enhancing the anchoring capability of WNO-MCS toward polysulfides.

To assess its potential in LSBs, separators were prepared by wet-coating WNO-MCS or MC onto commercial Celgard 2500 polypropylene (PP) membranes, denoted as WNO-MCS@PP and MC@PP, separately. The resulting WNO-MCS@PP separator shows excellent mechanical strength and interfacial adhesion, with no peeling observed after bending (Figure S9). SEM images (Figure S10) show a coating thickness of approximately 20.8 μm; both surface and cross-section views reveal a homogeneous structure, similar to that of MC@PP (Figure S11). Compared to the pristine PP and MC@PP separators, WNO-MCS@PP exhibits superior electrolyte wettability, with a contact angle near 0° (Figure S12), which promotes sulfur utilization and ion transport. The ability of the modified separators to suppress polysulfide shuttling was evaluated using an H-cell setup containing Li_2S_6 solution and blank electrolyte (Figure 2d). After 12 h of diffusion, the electrolyte on the right side of the cell with WNO-MCS@PP remained only light yellow, whereas the electrolytes with MC@PP and PP turned deep yellow and reddish-brown, respectively. These results confirm that WNO dispersed within the nitrogen-doped mesoporous carbon framework effectively inhibits LiPSs migration. The shuttle current test for different separators exhibits that the cell based on WNO-MCS presents the lowest shuttle current at the initial stage (Figure S13). And after 50 cycles, the increased extent in current density (3.6 μA cm^{-2}) is significantly less than that of MC (8.3 μA cm^{-2}) and PP (13.9 μA cm^{-2}), which further indicates that WNO-MCS can effectively inhibit the polysulfide shuttle. Charge density difference (CDD) analysis of WNO-MCS/Li_2S_6 and MC/Li_2S_6 (Figures 2e-i–ii and S14) using density functional theory (DFT) calculations shows enhanced electron transfer at the WNO surface, favoring stronger LiPSs adsorption on WNO-MCS than on MC, which is consistent with the calculated adsorption energies in Figure 2f (calculation details in the Supporting Information). Moreover, the vertically aligned 2D mesoporous channels exert a capillary-condensation effect that directs polysulfides toward the metallic active centers rather than the carbon matrix, synergistically suppressing shuttling and improving catalytic efficiency.

To investigate the efficacy of the catalyst in promoting the redox reaction, symmetric cells were prepared with the Li_2S_6 solution and WNO-MCS (or MC) electrodes. As illustrated in Figure 3a, the cyclic voltammetry (CV) curve of the cell with WNO-MCS electrodes at 5 mV s^{-1} exhibits high reversibility. Four well-defined peaks are observed at −0.23 V (peak a), −0.54 V (peak b), 0.23 V (peak c), and 0.54 V (peak d). Peaks a and b represent the stepwise reduction of Li_2S_8, while peaks c and d correspond to the reversible oxidation process [36]. The more pronounced peak separation and higher peak currents highlight the superior electrocatalytic activity of WNO-MCS in enhancing sulfur redox kinetics. Furthermore, electrochemical impedance spectroscopy (EIS) was conducted on the Li_2S_6 symmetric batteries. A smaller charge transfer resistance at the interface (Figure S15) indicates a more favorable reaction kinetics of WNO-MCS.

To quantify the migration ability of Li^+ in these modified separators, Li||Li symmetric cells were assembled to evaluate the Li^+ transference number (t_{Li^+}) using chronoamperometry measurement (Figures 3b and S16). Specifically, the WNO-MCS@PP separator exhibited the highest t_{Li^+} value of 0.42, compared to 0.32 for MC@PP and 0.21 for PP separators. Moreover, according to EIS analysis, the ionic conductivity (σ) of WNO-MCS@PP is 2.13×10^{-3} S cm^{-1}, superior to that of MC@PP (1.65×10^{-3} S cm^{-1}) and PP (1.28×10^{-3} S cm^{-1}) (Figure 3c). These results manifest that the in situ loaded WNO facilitates ion pair dissociation through strong interactions with LiPSs, and cooperates with 2D mesoporous channels possessing Li^+ sieving functionality to

15213757, 0, Downloaded from https://onlinelibrary.wiley.com/doi/10.1002/ange.9899225 by University Of Electronic Science And Technology Of China, Wiley Online Library on [24/04/2026]. See the Terms and Conditions (https://onlinelibrary.wiley.com/terms-and-conditions) on Wiley Online Library for rules of use; OA articles are governed by the applicable Creative Commons License

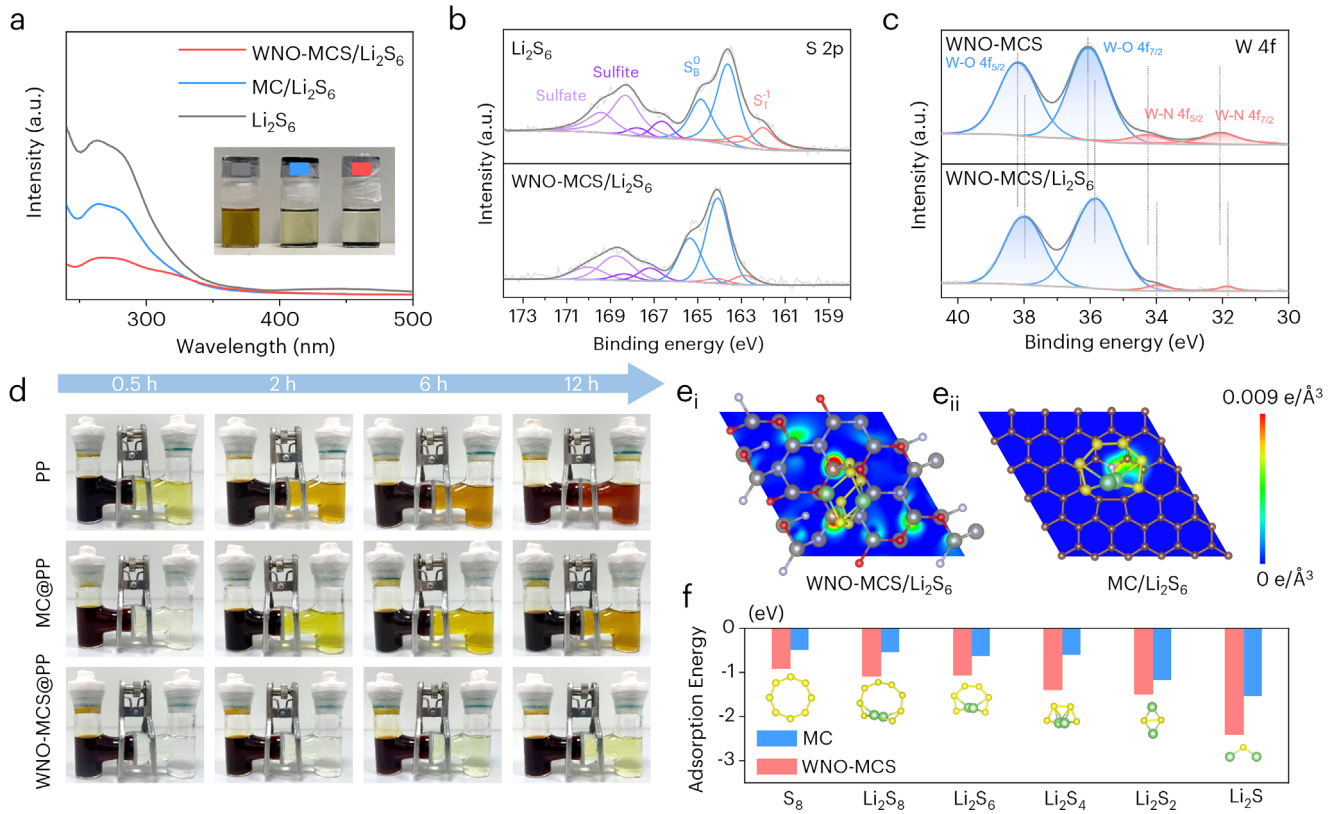

FIGURE 2 | The intrinsic chemical interactions of modifying agents adsorbing LiPSs. (a) UV-vis spectra of Li_2S_6 solutions after adding WNO-MCS and MC (inset: digital photograph of Li_2S_6 solution). XPS spectra of (b) S 2p and (c) W 4f of Li_2S_6 and WNO-MCS before and after adsorption with Li_2S_6. (d) H-type Li_2S_6-permeation experiments. The charge density difference of (e) (i) WNO-MCS/Li_2S_6 and (ii) MC/Li_2S_6. (f) First-principles calculation of the adsorption energies of LiPSs intermediates on WNO-MCS and MC.

accelerate rapid Li^+ migration synergistically. Figure 3d,e shows that during long-term cycling tests at 1 mA cm^{-2}, the symmetric cell with WNO-MCS@PP exhibited the lowest polarization overpotential, which followed an initial increase followed by a decrease. The increase in local overpotential can be attributed to the electrode surface undergoing the formation and reforming process of solid electrolyte interface (SEI) in the early stage, as well as the point aggregation of Li^+ caused by the tip effect [37, 38]. As the cycle progresses, the coating structure of WNO-MCS gradually achieves a uniform distribution of Li^+, and makes Li deposition/stripping smoother, thereby reducing overpotentials. On the contrary, the cell with PP is unable to effectively suppress the dendrite growth in the later stage of gradually increasing overpotential, resulting in a short circuit after 275 h. This phenomenon suggests that WNO-MCS endows LSBs with self-repair or self-optimization capabilities, thereby helping to extend the cycle life and stability of the batteries. Subsequently, the symmetric cells were disassembled to investigate the impact of the modified separators on Li anodes. Digital photographs reveal that the Li anode in the PP-based symmetric cell exhibits an extensive passivated surface of black "dead lithium" after cycling (Figure S17), resulting from the side reactions between Li dendrites and electrolyte [39]. Moreover, large particles and cracks are also observable in the corresponding SEM images. In contrast, the significantly smoother and flatter anode surface demonstrates the exceptional potential of WNO-MCS@ PP in suppressing Li dendrite formation (Figure 3f–h).

The galvanostatic intermittent titration technique (GITT) (Figures 4a and S18) was used to analyze the dynamic changes of internal resistance (IR) within the rated voltage range [40]. Accordingly, the corresponding IR profile (Figure 4b) provides insights into the sulfur redox processes in LSBs. In the initial discharge stage, the extensive generation of high viscosity long-chain LiPSs (Li_2S_x, where $4 \leq x \leq 8$) leads to an increase in resistance. The first peak (A) in the profile corresponds to the reduction of soluble long-chain LiPSs into insoluble short-chain LiPSs (Li_2S_x, where $2 \leq x \leq 4$). As the reaction proceeds, the accumulation of insoluble solid LiPSs on the electrode surface leads to a further increase in IR. The second peak (B) marks the rate-determining nucleation step involving the conversion of Li_2S_2 to Li_2S. Finally, the third peak (C) indicates the decomposition of Li_2S during the charging process. As the sulfur returns to its initial state, the IR drops significantly [41, 42]. Among all tested cells, the battery with the WNO-MCS@PP separator exhibits the lowest overall IR values, suggesting that the WNO-MCS catalysts promote Li-S reaction kinetics. This enhancement is attributed to heteroatom nitrogen doping and the synergistic effect of the dual active sites within the metal nanoparticles, which collectively optimize the kinetics of the sulfur reactions.

To further investigate the redox kinetics, potentiostatic discharge tests were performed using cells with a lithium anode, the catalyst material as the cathode, and a Li_2S_8 solution

15213757, 0, Downloaded from https://onlinelibrary.wiley.com/doi/10.1002/ange.9899225 by University Of Electronic Science And Technology Of China, Wiley Online Library on [24/04/2026]. See the Terms and Conditions (https://onlinelibrary.wiley.com/terms-and-conditions) on Wiley Online Library for rules of use; OA articles are governed by the applicable Creative Commons License

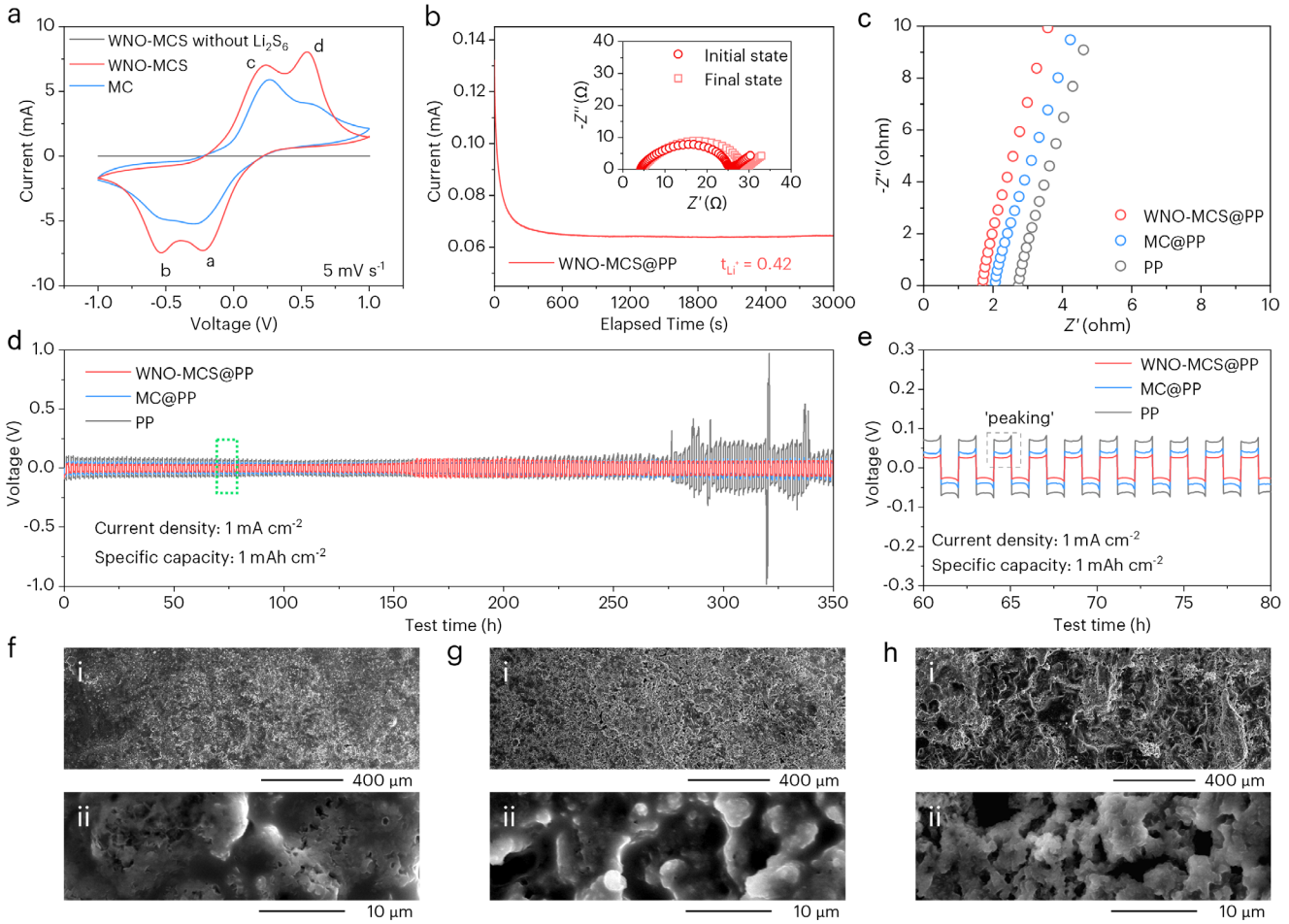

FIGURE 3 | Li-S reaction kinetics analysis based on symmetric cell. (a) CV profiles of the symmetric cells with the WNO-MCS and MC-based electrodes. (b) Chronoamperometric curve of the Li||Li symmetric cells with the WNO-MCS@PP separator (inset: the corresponding EIS plot). (c) EIS plots estimating Li^+ conductivity of the symmetric cells. (d) Cycling stability of symmetric cells and (e) corresponding partial profile marked with a green dotted line. SEM images of the Li electrode surface based on (f) WNO-MCS@PP, (g) MC@PP, and (h) PP (ii is the partial enlarged view of the corresponding i).

electrolyte (Figure 4c). Compared with MC, the WNO-MCS-based cell exhibits a higher Li_2S nucleation capacity (289.5 vs. 174.3 mAh g^{-1}), more favorable nucleation kinetics (9.4×10^{-4} vs. 3.6×10^{-4} s^{-1}, K_{eff}: effective reaction rate constant) [43], and a shorter response time to reach the peak (1360 vs. 1529 s). The exchange current density (i_0) and tafel slope (k_t), derived from linear sweep voltammetry (LSV, Figure S19a) using Butler–Volmer fitting, provide insights into the solid–liquid conversion kinetics. As shown in Figures 4d and S19b, WNO-MCS@PP exhibits a higher i_0 (0.057 mA cm^{-2}) and a lower k_t (66.2 mV dec^{-1}) than MC@PP (0.031 mA cm^{-2}, 88.3 mV dec^{-1}) and PP (0.012 mA cm^{-2}, 125.1 mV dec^{-1}), indicating faster charge transfer kinetics at the electrode–electrolyte interface. Benefiting from this enhanced kinetics, the LSB with a WNO-MCS-modified separator shows higher reduction peak potentials (peaks A and B) and a lower oxidation peak potential (peak C) in the CV profile (Figure 4e). Moreover, as the scan rate increases from 0.1 to 0.5 mV s^{-1} (Figures 4f and S20), the Li^+ diffusion coefficients (D_{Li+}, in units of 10^{-10} cm^2 s^{-1}) for the WNO-MCS@PP cell at peaks A, B, and C are calculated to be 0.30, 1.69, and 1.97, respectively, higher than those for MC@PP (0.17, 0.69, 1.62) and PP (0.15, 0.58, 1.30). These results confirm that WNO-MCS reduces polarization and accelerates polysulfide conversion kinetics. Resistance characteristics further influence cell polarization. Fitted Nyquist plots using an appropriate equivalent circuit (Figure 4g) reveal that the WNO-MCS-modified cell has the smallest charge-transfer resistance (R_{ct} = 20.9 Ω), compared to MC@PP (47.7 Ω) and PP (61.3 Ω). The sulfur reduction reaction (SRR) activity on WNO and MC surfaces for each reduction step from S_8 to Li_2S was also evaluated by DFT calculations of the Gibbs free energy change (calculation details in the Supporting Information). As shown in Figure 4h, the free energy decreases during $S_8 \rightarrow Li_2S_8 \rightarrow Li_2S_6$ (exergonic) and increases in subsequent reduction steps (endergonic). The lower decomposition energy barrier for polysulfides on the WNO surface compared to that on the N-doped graphene-like surface of MC indicates that WNO catalysts can effectively promote sulfur reaction kinetics during charging, thereby accelerating sulfur conversion and strongly suppressing the shuttle effect of soluble LiPSs [44, 45].

Based on the above findings, WNO-MCS proves to be a highly effective multifunctional separator modifier, capable of both suppressing the shuttling of LiPSs while catalyzing their rapid conversion. Figure 5a compares the rate performance of the

15213757, 0, Downloaded from https://onlinelibrary.wiley.com/doi/10.1002/ange.9899225 by University Of Electronic Science And Technology Of China, Wiley Online Library on [24/04/2026]. See the Terms and Conditions (https://onlinelibrary.wiley.com/terms-and-conditions) on Wiley Online Library for rules of use; OA articles are governed by the applicable Creative Commons License

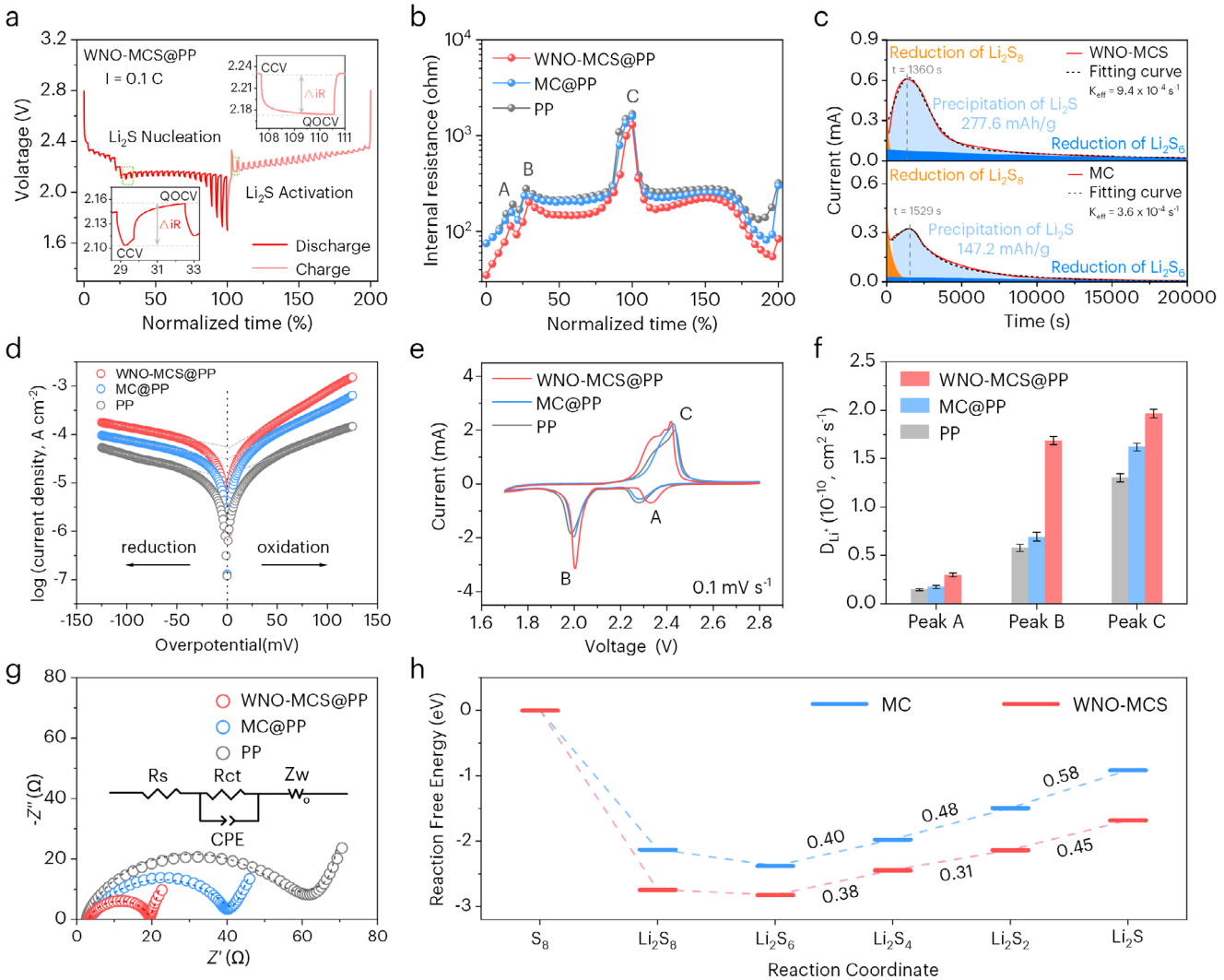

FIGURE 4 | Li-S reaction kinetics analysis based on full-cell (a) GITT profiles of LSBs with WNO-MCS@PP (QOCV: quasi-open-circuit voltage, and CCV: closed-circuit voltage). (b) Internal reaction resistances calculated from the GITT curve with various separators. (c) Potentiostatic nucleation curves of Li_2S with WNO-MCS and MC. (d) Tafel plots and (e) CV curves of LSBs with different separators. (f) Li^+ diffusion coefficient based on peaks A, B, and C from the CV curves. (g) EIS of LSBs with different separators (inset: equivalent circuit used for fitting). (h) Reaction free energy change for the discharging process from S_8 to Li_2S at the MC and WNO-MCS.

three different LSBs. The cell equipped with the WNO-MCS-modified separator delivered exceptional primary discharge capacity (1424.6 mAh g^{-1} at 0.2 C) and high-rate performance (798.4 mAh g^{-1} at 5 C) across a wide range of current densities. As the current density was returned to 0.5 C, an impressive reversible capacity of 1066.4 mAh g^{-1} was restored. In contrast, cells with MC@PP and PP separators show markedly lower capacities at high rates, reflecting their slower reaction kinetics. The related galvanostatic charge-discharge (GCD) plots (Figure S21) clearly reveal that the WNO-MCS-based cell maintains stable voltage platforms, even under high rates, confirming the accelerated electrochemical reaction stemming from the WNO-MCS electrocatalyst. The WNO-MCS@PP cell also exhibits superior long-term cycling stability. At 0.5 C (Figure S22), it delivered an original performance of 1262.7 mAh g^{-1} and preserved 904.4 mAh g^{-1} after 200 cycles. These values are markedly exceed those of the MC@PP (1153.8 mAh g^{-1} initial, 745.9 mAh g^{-1} after 200 cycles) and the PP cell (868.1 mAh g^{-1} initial, 435.3 mAh g^{-1} after 200 cycles). Moreover, thanks to its excellent anti-polarization capability, the WNO-MCS-based cell exhibits the lowest voltage difference (ΔE) separating the charging and discharging voltage platforms (Figure 5b).

For practical implementation, LSBs must maintain stable performance under diverse and demanding conditions. First, the self-discharge behavior was evaluated (Figure 5c). The WNO-MCS-based cell retains 95.8% of its capacity after 72 h of rest, significantly outperforming cells with MC@PP (87.1%) and PP (68.8%) separators (Figure S23). Moreover, at an elevated temperature of 60°C, the cell with WNO-MCS@PP exhibits fast redox kinetics and strong polysulfide adsorption, delivering a capacity of 946.7 mAh g^{-1} after 100 cycles at 0.2 C (Figure 5d). In contrast, under the same conditions, the PP-based cell suffers from severe shuttle effect and loses most of its discharge capacity within 50 cycles. In the presence of a lean electrolyte (E/S = 6.2 μL mg^{-1}), the WNO-MCS catalyst enables stable cycling with a coulombic efficiency exceeding 98%, along with significantly improved capacity retention and cycling stability (Figure 5e).

15213757, 0, Downloaded from https://onlinelibrary.wiley.com/doi/10.1002/ange.9899225 by University Of Electronic Science And Technology Of China, Wiley Online Library on [24/04/2026]. See the Terms and Conditions (https://onlinelibrary.wiley.com/terms-and-conditions) on Wiley Online Library for rules of use; OA articles are governed by the applicable Creative Commons License

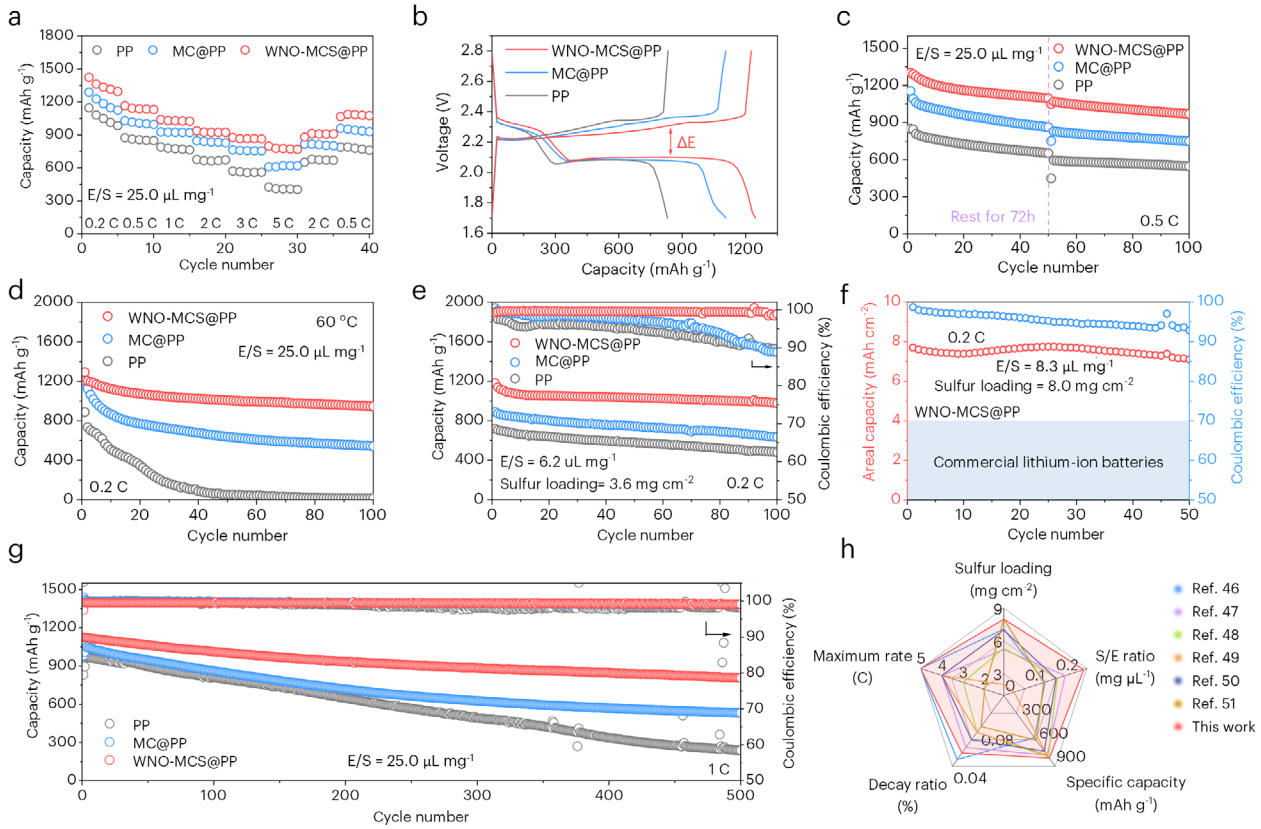

FIGURE 5 | Performance of the Li-S coin cells. (a) Rate performance of different cells. (b) GCD curves at 0.5 C. (c) Self-discharge evaluation of different cells. Cyclic performance of different cells under (d) high−temperature environment of 60°C and (e) conditions of poor electrolyte. (f) Cycling performance of the cell with WNO-MCS@PP under high sulfur loading of 8.0 mg cm^{-2}. (g) Cycling performance of different cells at 1 C. (h) The key performance comparison between our work and recently reported works.

The performance of the WNO-MCS-based cell was also assessed under high sulfur loading. At a sulfur loading of 8.0 mg cm^{-2}, the cell achieves an area-specific capacity of 7.7 mAh cm^{-2} initially and maintains 7.1 mAh cm^{-2} after 50 cycles at 0.2 C, demonstrating excellent sulfur utilization and high catalytic activity (Figure 5f). Furthermore, during long-term cycling at 1 C, the WNO-MCS-based cell consistently delivers higher discharge capacities with a minimal capacity fading of merely 0.054% each cycle (Figure 5g), indicating effective suppression of the shuttle effect and enhanced sulfur conversion. These results are highly competitive compared with recent reports, particularly under demanding conditions such as low E/S ratios and high sulfur loadings (Figure 5h) [46–51]. Overall, the findings confirm the superior ability of the WNO-MCS electrocatalyst to mitigate polysulfide shuttling and accelerate redox kinetics in practical LSBs.

Inspired by the remarkable outcomes of coin-type configurations, a Li-S pouch cell was constructed following the structure illustrated in Figure 6a and evaluated under long-term cycling conditions. Figure 6b displays the performance of the pouch cell employing the WNO-MCS@PP separator. Under a sulfur areal loading of about 3.9 mg cm^{-2} and a lean E/S ratio of 3.5 mL g^{-1}, the cell delivers an initial discharge capacity of 0.62 Ah (corresponding to 1075.9 mAh g^{-1}) at 0.05 C, while maintaining a reversible capacity of 0.42 Ah (714.1 mAh g^{-1}) after 100 cycles. The associated GCD curves (Figure 6c) demonstrate that the pouch cell maintains an average operating voltage around 2.1 V throughout cycling, consistent with the voltage measured by a multimeter (Figure 6d-i). The cell achieves an energy density of 360 Wh kg^{-1}, calculated based on the total mass of the cathode, anode, separator, and electrolyte (3.71 g) [52]. Moreover, after cycling, the pouch cell continues to power an LED lamp even under bending or cutting conditions (Figure 6d-ii–iv), highlighting its outstanding operational stability and safety. These results provide strong evidence for the feasibility of constructing high-performance, practical LSBs.

3 | Conclusions

In summary, a multifunctional two-dimensional tungsten oxynitride-mesoporous carbon nanosheet (WNO-MCS) modifier for separators has been successfully designed and synthesized via a self-template interfacial assembly strategy. Experimental results and theoretical calculations confirm that the spatial confinement effect leads to a uniform distribution of ultrafine WNO nanoclusters (~2.9 nm) within the mesoporous channels, substantially increasing the density of exposed active sites. Moreover, the high specific surface area (588.7 m^2 g^{-1}) and unique 2D mesostructure with 3.9 nm pores provide abundant regions for LiPSs adsorption, thus effectively mitigating the polysulfide shuttle and accelerating redox processes through strong binding interactions and reduced conversion energy barriers. Benefiting from these structural advantages, LSBs equipped with WNO-MCS-modified separators deliver outstanding electrochemical

15213757, 0, Downloaded from https://onlinelibrary.wiley.com/doi/10.1002/ange.9899225 by University Of Electronic Science And Technology Of China, Wiley Online Library on [24/04/2026]. See the Terms and Conditions (https://onlinelibrary.wiley.com/terms-and-conditions) on Wiley Online Library for rules of use; OA articles are governed by the applicable Creative Commons License

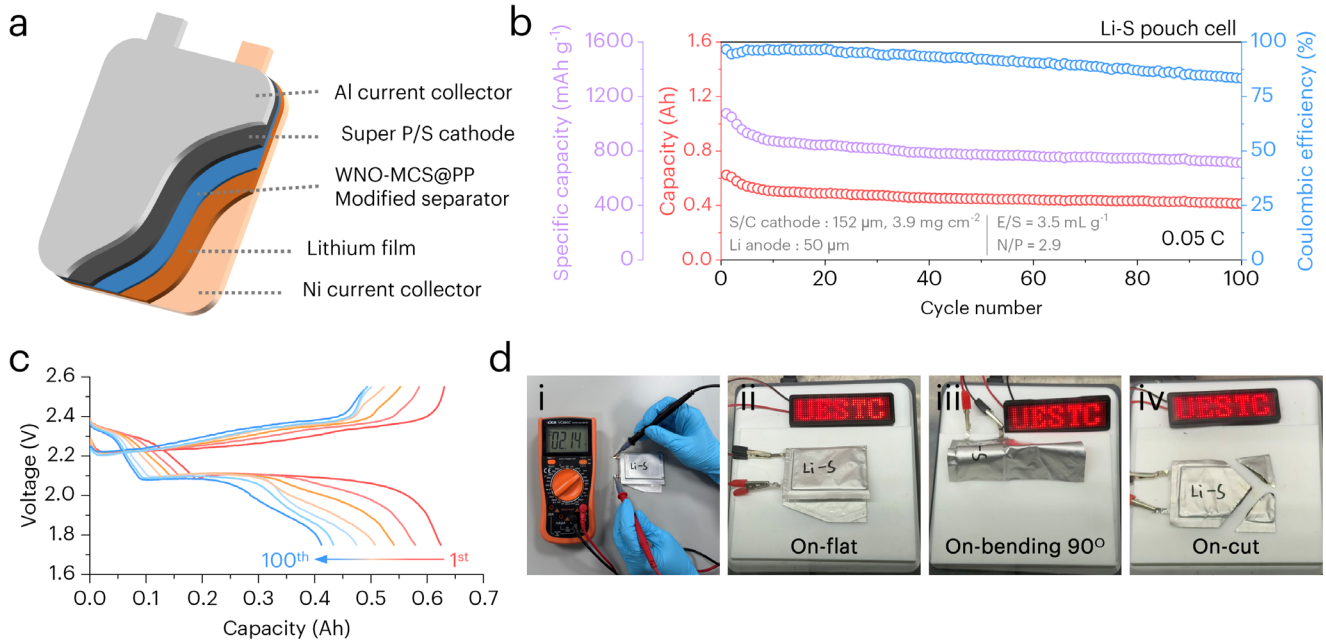

FIGURE 6 | Performance of the Li-S pouch cell. (a) Diagram of the Li-S pouch cell structure. (b) Cycling performance of the pouch cell at 0.05 C. (c) The corresponding voltage curves. (d) Digital photographs of the pouch cell after cycling under various conditions. (i) Open-circuit voltage without load. Lighting LED lamp on (ii) flat, (iii) bending 90°, and (iv) cutting conditions.

performance: a superior specific capacity of 798.4 mAh g^{-1} at 5 C, a capacity fading of merely 0.054% each cycle over 500 cycles at 1 C, and stable long-term cycling with a coulombic efficiency exceeding 98% for an E/S ratio of 6.2 μL mg^{-1}. Additionally, an impressive areal capacity of 7.7 mAh cm^{-2} is achieved at the sulfur loading of 8.0 mg cm^{-2}, with a reversible capacity of 7.1 mAh cm^{-2} after 50 cycles at 0.2 C, representing a preservation of 92%. Remarkably, the assembled Li-S pouch cell delivers a starting discharge capacity of 0.62 Ah and a high energy density of 360 Wh kg^{-1}. These metrics underscore the promising application potential of the 2D WNO-MCS architecture in high-performance LSBs.

Acknowledgments

This work is supported by National Natural Science Foundation of China (22475031), National Youth Top-notch Talent Support Program of China, Sichuan Science and Technology Program (2025NSFTD0003), and the Center for HPC at the University of Electronic Science and Technology of China. It uses computational resources provided by the Hefei Advanced Computing Center.

Conflicts of Interest

The authors declare no conflicts of interest.

Data Availability Statement

Research data are not shared.

References

1. S. Bai, X. Liu, K. Zhu, S. Wu, and H. Zhou, "Metal–Organic Framework-Based Separator for Lithium–Sulfur Batteries," *Nature Energy* 1 (2016): 16094.

2. Y.-H. Liu, L.-X. Li, A.-Y. Wen, F.-F. Cao, and H. Ye, "A Janus MXene/MOF Separator for the All-in-One Enhancement of Lithium-Sulfur Batteries," *Energy Storage Materials* 55 (2023): 652.

3. M. Zhao, "The Pursuit for Practical Lithium-Sulfur Batteries," *Chemistry* 6 (2020): 3161.

4. R. Liu, X. Pan, Z. Xu, et al., "Sustainable Poly Thioctic Acid-Based Elastomer for Super-Stretchable Electronic Sensors," *Advanced Functional Materials* 35 (2025): e12794.

5. W. Yao, C. Tian, C. Yang, et al., "P-Doped $NiTe_2$ With Te-Vacancies in Lithium–Sulfur Batteries Prevents Shuttling and Promotes Polysulfide Conversion," *Advanced Materials* 34 (2022): 2106370.

6. M. Waqas, Y. Niu, M. Tang, et al., "A Decade of Development in Cathode-facing Surface Modified Separators for High-Performance Li-S Batteries," *Energy Storage Materials* 72 (2024): 103682.

7. L. Ma, Y. Zhang, S. Zhang, et al., "Integrating Energy Band Alignment and Oxygen Vacancies Engineering of TiO_2 Anatase/Rutile Homojunction for Kinetics-Enhanced Li–S Batteries," *Advanced Functional Materials* 33 (2023): 2305788.

8. Y. Chen, T. Wang, H. Tian, D. Su, Q. Zhang, and G. Wang, "Advances in Lithium–Sulfur Batteries: From Academic Research to Commercial Viability," *Advanced Materials* 33 (2021): 2003666.

9. T. Wang, J. He, X.-B. Cheng, J. Zhu, B. Lu, and Y. Wu, "Strategies Toward High-Loading Lithium–Sulfur Batteries," *ACS Energy Letters* 8 (2023): 116.

10. C. Wei, B. Xi, P. Wang, et al., "In Situ Anchoring Ultrafine ZnS Nanodots on 2D MXene Nanosheets for Accelerating Polysulfide Redox and Regulating Li Plating," *Advanced Materials* 35 (2023): 2303780.

11. M. Xu, Q. Zhu, Y. Li, Y. Gao, N. Sun, and B. Xu, "Atom-dominated Relay Catalysis of High-entropy MXene Promotes Cascade Polysulfide Conversion for Lithium–sulfur Batteries," *Energy & Environmental Science* 17 (2024): 7735.

12. H. Xu, Q. Jiang, K. S. Hui, et al., "Interfacial 'Double-Terminal Binding Sites' Catalysts Synergistically Boosting the Electrocatalytic Li_2S Redox for Durable Lithium–Sulfur Batteries," *ACS Nano* 18 (2024): 8839.

13. F. Pei, L. Lin, D. Ou, et al., "Self-Supporting Sulfur Cathodes Enabled by Two-Dimensional Carbon Yolk-Shell Nanosheets for High-Energy-

15213757, 0, Downloaded from https://onlinelibrary.wiley.com/doi/10.1002/ange.9899225 by University Of Electronic Science And Technology Of China, Wiley Online Library on [24/04/2026]. See the Terms and Conditions (https://onlinelibrary.wiley.com/terms-and-conditions) on Wiley Online Library for rules of use; OA articles are governed by the applicable Creative Commons License

Density Lithium-Sulfur Batteries," *Nature Communications* 8 (2017): 482.

14. H. M. Kim, J.-Y. Hwang, S. Bang, et al., "Tungsten Oxide/Zirconia as a Functional Polysulfide Mediator for High-Performance Lithium–Sulfur Batteries," *ACS Energy Letters* 5 (2020): 3168.

15. H. Lin, S. Zhang, T. Zhang, et al., "Elucidating the Catalytic Activity of Oxygen Deficiency in the Polysulfide Conversion Reactions of Lithium–Sulfur Batteries," *Advanced Energy Materials* 8 (2018): 1801868.

16. Y. Xiao, Y. Feng, X. Huang, K. Niu, H. Liu, and W. Li, "Ultrathin Mesoporous Nanosheet-Nanoconfined Low-Crystallinity Framework Membranes for Ultrafast and Highly Selective Hydrogen Separation," *Advanced Functional Materials* 35 (2025): 2421913.

17. Y. Cui, K. Xiao, N. M. Bedford, et al., "Refilling Nitrogen to Oxygen Vacancies in Ultrafine Tungsten Oxide Clusters for Superior Lithium Storage," *Advanced Energy Materials* 9 (2019): 1902148.

18. S. Choi, D. H. Seo, M. R. Kaiser, et al., "WO_3 Nanolayer Coated 3D-Graphene/Sulfur Composites for High Performance Lithium/Sulfur Batteries," *Journal of Materials Chemistry A* 7 (2019): 4596.

19. B. Wang, K. Chen, J. Liang, Z. Yu, D.-W. Wang, and R. Fang, "Lithium Cation-Doped Tungsten Oxide as a Bidirectional Nanocatalyst for Lithium-sulfur Batteries With High Areal Capacity," *Journal of Energy Chemistry* 98 (2024): 406.

20. X. Chen, Z. Xiao, X. Ning, et al., "Sulfur-Impregnated, Sandwich-Type, Hybrid Carbon Nanosheets With Hierarchical Porous Structure for High-Performance Lithium-Sulfur Batteries," *Advanced Energy Materials* 4 (2014): 1301988.

21. Y. Zhu, S. Yang, Z. Wei, H. He, Y. Zhu, and J. Zhu, "Revealing Dynamic Sulfidation of WC-WO_3 Heterogeneous Nanoparticles: In Situ Formation of WS_2 Facilitates Sulfur Redox in Li–S Battery," *Carbon* 232 (2025): 119790.

22. B. Zhang, C. Luo, Y. Deng, et al., "Optimized Catalytic WS_2–WO_3 Heterostructure Design for Accelerated Polysulfide Conversion in Lithium–Sulfur Batteries," *Advanced Energy Materials* 10 (2020): 2000091.

23. M. Yu, Y. Han, X. Cheng, et al., "Holey Tungsten Oxynitride Nanowires: Novel Anodes Efficiently Integrate Microbial Chemical Energy Conversion and Electrochemical Energy Storage," *Advanced Materials* 27 (2015): 3085.

24. H. Fu, Y. Wu, L. Wang, et al., "Mirror-Symmetric Nanoarray Networks of Atomic Ni-Incorporated Tungsten Oxynitride for Efficient and Robust Alkaline Hydrogen Evolution," *Angewandte Chemie International Edition* 64 (2025): e18043.

25. J. Han, X. Meng, L. Lu, J. Bian, Z. Li, and C. Sun, "Single-Atom Fe-N_x-C as an Efficient Electrocatalyst for Zinc–Air Batteries," *Advanced Functional Materials* 29 (2019): 1808872.

26. H. Yu, X. Yang, X. Xiao, et al., "Atmospheric-Pressure Synthesis of 2D Nitrogen-Rich Tungsten Nitride," *Advanced Materials* 30 (2018): 1805655.

27. H. Wang, E. J. Sandoz-Rosado, S. H. Tsang, et al., "Elastic Properties of 2D Ultrathin Tungsten Nitride Crystals Grown by Chemical Vapor Deposition," *Advanced Functional Materials* 29 (2019): 1902663.

28. Z. Huang, B. Yang, Y. Zhou, et al., "Tungsten Nitride/Tungsten Oxide Nanosheets for Enhanced Oxynitride Intermediate Adsorption and Hydrogenation in Nitrate Electroreduction to Ammonia," *ACS Nano* 17 (2023): 25091.

29. S. B. Patil, R. P. Nikam, V. C. Lokhande, C. D. Lokhande, and R. S. Patil, "Tungsten Oxide/Reduced Graphene Oxide Composite Electrodes for Solid-state Asymmetric Supercapacitor Application," *Advanced Composites Hybrid Materials* 8 (2025): 175.

30. Z. Huang, D. Ma, P. Nian, et al., "Coordinating Interface Polymerization With Micelle Mediated Assembly Towards Two-Dimensional Mesoporous Carbon/CoNi for Advanced Lithium–Sulfur Battery," *Small* 19 (2023): 2207411.

31. S. Wang, L. Li, Y. Shao, et al., "Transition-Metal Oxynitride: A Facile Strategy for Improving Electrochemical Capacitor Storage," *Advanced Materials* 31 (2019): 1806088.

32. U. Jeong, H. Kim, S. Ramesh, et al., "Rapid Access to Ordered Mesoporous Carbons for Chemical Hydrogen Storage," *Angewandte Chemie International Edition* 60 (2021): 22478.

33. M. Zhao, H. Peng, Z. Zhang, et al., "Activating Inert Metallic Compounds for High-Rate Lithium–Sulfur Batteries through in Situ Etching of Extrinsic Metal," *Angewandte Chemie International Edition* 58 (2019): 3779.

34. J. Yu, O. Usoltsev, I. Martynova, et al., "Promoting Electrochemical Reactions With Dual-Atom Catalysts for High-Rate Lithium–Sulfur Batteries," *Advanced Materials* 38 (2026): e11345.

35. G. Li, W. Lei, D. Luo, et al., "Stringed 'Tube on Cube' Nanohybrids as Compact Cathode Matrix for High-Loading and Lean-Electrolyte Lithium–Sulfur Batteries," *Energy & Environmental Science* 11 (2018): 2372.

36. L. Zhang, D. Liu, Z. Muhammad, et al., "Single Nickel Atoms on Nitrogen-Doped Graphene Enabling Enhanced Kinetics of Lithium–Sulfur Batteries," *Advanced Materials* 31 (2019): 1903955.

37. H. Dai, X. Gu, J. Dong, C. Wang, C. Lai, and S. Sun, "Stabilizing Lithium Metal Anode by Octaphenyl Polyoxyethylene-Lithium Complexation," *Nature Communications* 11 (2020): 643.

38. E. Cha, M. D. Patel, J. Park, et al., "2D MoS_2 as an Efficient Protective Layer for Lithium Metal Anodes in High-performance Li–S Batteries," *Nature Nanotechnology* 13 (2018): 337.

39. C. Jin, T. Liu, O. Sheng, et al., "Rejuvenating Dead Lithium Supply in Lithium Metal Anodes by Iodine Redox," *Nature Energy* 6 (2021): 378.

40. W. Yang, D. You, Z. Ni, et al., "Construction of an Adsorption-Diffusion Model Reveals the Conversion-Deposition Process of Polysulfides," *Green Energy and Environment* 10 (2025): 1911.

41. Y. Kong, X. Ao, X. Huang, et al., "Ni-CeO_2 Heterostructures in Li-S Batteries: A Balancing Act Between Adsorption and Catalytic Conversion of Polysulfide," *Advancement of Science* 9 (2022): 2105538.

42. C. Zhao, Y. Liu, F. Huo, et al., "Synergistic Catalysts for Lithium-Sulfur Batteries: Ni Single Atom and MoC Nanoclusters Composites," *Angewandte Chemie International Edition* 64 (2025): e202502177.

43. J. Yu, I. Martynova, Z. Li, et al., "Electrochemical Nucleation and Growth in Battery Electrodes Under Reactant-Limited Conditions," *Nano Letters* 26 (2026): 1534.

44. H. Lu, Y. Su, X. Zhang, et al., "Synergistic Adsorption-Diffusion-Catalytic Effect Boosting Polysulfides Conversion by Rational Isotype Heterojunction Design for Highly Reversible Lithium–Sulfur Batteries," *Advanced Functional Materials* 35 (2025): 2425863.

45. X. Sun, Y. Qiu, B. Jiang, et al., "Isolated Fe-Co Heteronuclear Diatomic Sites as Efficient Bifunctional Catalysts for High-Performance Lithium-Sulfur Batteries," *Nature Communications* 14 (2023): 291.

46. X. Li, Q. Guan, Z. Zhuang, et al., "Ordered Mesoporous Carbon Grafted MXene Catalytic Heterostructure as Li-Ion Kinetic Pump Toward High-Efficient Sulfur/Sulfide Conversions for Li–S Battery," *ACS Nano* 17 (2023): 1653.

47. Y. Zhang, X. Zhang, G. Liu, et al., "Accelerating Sulfur Conversion Kinetics by Topological Semimetal Electrocatalysts Pd_3Sn for High-Performance Li-S Batteries," *Advanced Functional Materials* 35 (2025): 2417750.

48. M. Lu, T. Yan, Y. Ding, et al., "Theory-Guided Optimization of Coordination Sites via D-Band Modulation for Efficient Single-Atomic Li–S Catalysis," *Energy Storage Materials* 70 (2024): 103458.

49. P. Chen, T. Huang, T. Wei, B. Ding, H. Dou, and X. Zhang, "Enhanced Transformation Kinetics of Polysulfides Enabled by Synergistic Catalysis of Functional Graphitic Carbon Nitride for High-Performance Li-S Batteries," *Advanced Functional Materials* 35 (2025): 2420351.

15213757, 0, Downloaded from https://onlinelibrary.wiley.com/doi/10.1002/ange.9899225 by University Of Electronic Science And Technology Of China, Wiley Online Library on [24/04/2026]. See the Terms and Conditions (https://onlinelibrary.wiley.com/terms-and-conditions) on Wiley Online Library for rules of use; OA articles are governed by the applicable Creative Commons License

50. J. Feng, C. Zhang, W. Liu, et al., "Enabling Efficient Anchoring-Conversion Interface by Fabricating Double-Layer Functionalized Separator for Suppressing Shuttle Effect," *Angewandte Chemie International Edition* 63 (2024): e07042.

51. X. Liu, X. Sun, R. Yan, et al., "Structural and Functional Optimization of Lithium-Sulfur Battery Separators by Sulfur-Containing of Covalent Organic Frameworks," *Advanced Functional Materials* 35 (2025): 2505986.

52. J. Wang, X. Zhang, J. Liu, et al., "High-Spin Cobalt Enables Strong Metal-Sulfur Orbital Hybridization for Accelerated Polysulfide Conversion in Lithium-Sulfur Batteries," *Advanced Materials* 37 (2025): 2502075.

Supporting Information

Additional supporting information can be found online in the Supporting Information section.

Supporting File 1: ange72346-sup-0001-SuppMat.docx.

15213757, 0, Downloaded from https://onlinelibrary.wiley.com/doi/10.1002/ange.9899225 by University Of Electronic Science And Technology Of China, Wiley Online Library on [24/04/2026]. See the Terms and Conditions (https://onlinelibrary.wiley.com/terms-and-conditions) on Wiley Online Library for rules of use; OA articles are governed by the applicable Creative Commons License